Nonlinear triggering process of whistler-mode emissions in a homogeneous magnetic field

AUTHOR(S):

Fujiwara, Yuya; Nogi, Takeshi; Omura, Yoshiharu

Fujiwara *et al. Earth, Planets and Space* (2022) 74:95
https://doi.org/10.1186/s40623-022-01646-x

Earth, Planets and Space

FULL PAPER Open Access

Nonlinear triggering process of whistler-mode emissions in a homogeneous magnetic field

Yuya Fujiwara*, Takeshi Nogi and Yoshiharu Omura

Abstract

We perform an electromagnetic particle simulation of triggered emissions in a uniform magnetic field for understanding of nonlinear wave–particle interaction in the vicinity of the magnetic equator. A finite length of a whistler-mode triggering wave packet with a constant frequency is injected by oscillating an external current at the equator. We find that the first subpacket of triggered emissions is generated in the homogeneous magnetic field. By analyzing resonant currents and resonant electron dynamics in the simulation, we find that the formation of an electron hole in a velocity phase space results in resonant currents, and the currents cause wave amplification and frequency increase. We obtain the interaction time of counter-streaming resonant electrons in a triggering wave packet with a finite width. By changing the duration time of the triggering pulse, we evaluate the interaction time necessary for formation of an electron hole. We conduct 4 runs with different duration times of the triggering pulse, 980, 230, 105, 40 Ω_e^{-1}, which correspond to cases with interaction times, 370%, 86%, 39%, and 15% of the nonlinear trapping period, respectively. We find generation of triggered emissions in the three cases of 370%, 86%, and 39%, which agrees with the conventional nonlinear model that the nonlinear transition time, which is necessary for formation of resonant currents, is about a quarter of the nonlinear trapping period.

Keywords: Wave–particle interaction, Whistler-mode waves, Triggered emissions, Cyclotron resonance, Phase-bunching, Particle simulation

*Correspondence: fujiwara.yuya.53v@kyoto-u.jp

Research Institute for Sustainable Humanosphere, Kyoto University, Uji, Kyoto 611-0011, Japan

Graphic Abstract

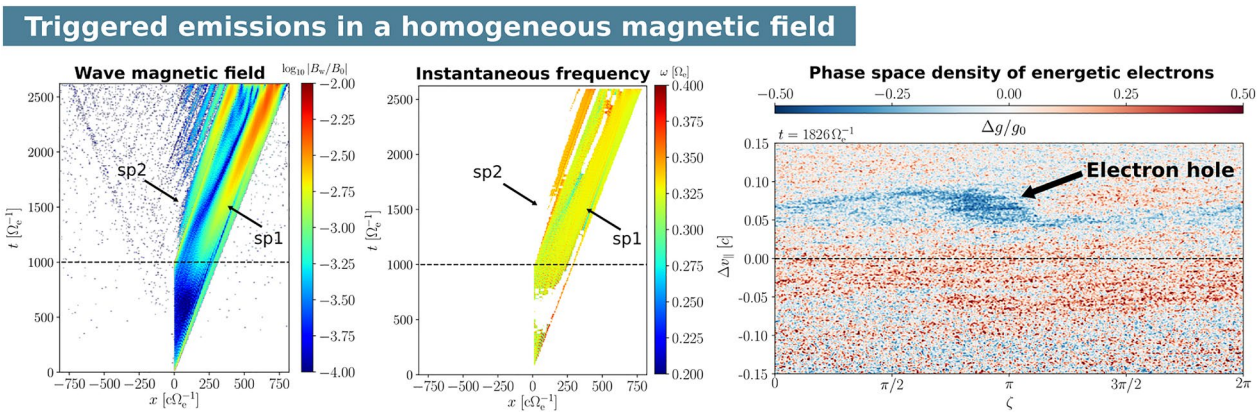

Introduction

VLF triggered emission is a secondary emission triggered by natural whistler-mode waves or man-made signals in the magnetosphere (e.g., Helliwell 1988a). Triggered emissions are characterized by a variety of phenomena, including nonlinear wave amplification, frequency variation, and pitch angle scattering of energetic electrons. It has been pointed out that these features and the generation process of triggered emissions are the same as those of chorus emissions (Helliwell et al. 1986; Helliwell 1988b). Nonlinear wave–particle interaction via cyclotron resonance plays an important role in the generation mechanism. It is helpful to reproduce the triggered emissions for understanding of nonlinear generation process of chorus emissions, which play an important role in the formation process of radiation belt electrons by local acceleration (e.g., Baker et al. 2018).

Active experiments of triggered emissions have been conducted. The results of previous active experiments were reviewed by Gołkowski et al. (2019). Whistler-mode waves injected from VLF communication transmitters to the magnetosphere travel along the Earth's magnetic field line, and a VLF receiver observes the injected waves and triggered waves at the magnetic conjugate point. Although ground-based observations are useful for describing wave phenomena and the macroscopic physics of the real space plasma, it is difficult to analyze microscopic physics such as gyroresonant electrons dynamics. Numerical experiments have also been performed for understanding the nonlinear and microscopic process of wave–particle interaction. Nunn et al. (1999) simulated risers, fallers, and hooks by a Vlasov hybrid simulation code. Katoh and Omura (2006) have developed an electromagnetic electron hybrid code and reproduced rising-tone triggered emissions successfully, showing the effect of resonant currents on the generation of triggered emissions. Hikishima et al. (2010) reproduced rising-tone triggered emissions by using a full particle simulation code, and a clear structure of an electron hole was observed in the simulation (Hikishima and Omura 2012). In a recent study, falling-tone triggered emissions were reproduced by the full particle simulation code (Nogi et al. 2020). Rising-tone magnetosonic waves by ring distribution protons in a uniform magnetic field were simulated using PIC simulations (Sun et al. 2020). A numerical simulation based on the nonlinear equations describing the magnetospheric backward wave oscillator regime (Trakhtengerts et al. 2003) was conducted by Demekhov (2011), who found generation of rising tones and falling tones due to bounce oscillations of phase-bunched energetic electrons. A computational and theoretical analysis of falling-tone emissions was also conducted by Nunn and Omura (2012) based on the Vlasov hybrid simulation.

The nonlinear wave growth theory has been developed in parallel with the active and numerical experiments. The summary paper of the theoretical developments has been published recently (Omura 2021). The presence of an electron hole or hill in the velocity phase space forms the resonant currents, and resonant currents amplify the magnitude of triggered emissions and change their frequencies. Nonlinear wave growth by resonant currents takes place near the magnetic equator as an absolute instability and generate a new wave packet. The wave packet triggered near the equator grows through propagation in the downstream region because of the increasing gradient of the magnetic field and the growing wave amplitude, both of which can keep the asymmetric

electron hole forming nonlinear resonant currents for wave growth. This nonlinear wave growth process through propagation away from the equator was confirmed in a recent simulation study with an inhomogeneous magnetic field (Nogi and Omura 2022).

In this paper, we reproduce the triggered emission by using a self-consistent electromagnetic particle simulation to confirm whether it is possible to generate the first subpacket of the triggered emission without the magnetic field gradient . By comparing results with different lengths of the triggering wave packet, we confirm the minimum length and the interaction time for generation of the triggered emissions. We also reveal the formation process of the electron hole by following the resonant electrons dynamics. This paper is organized as follows. We describe the simulation model and the initial condition for the plasma environment in "Simulation model" section. Characteristics of reproduced triggered emissions is shown in "Triggered emissions in a uniform magnetic field" section. We demonstrate the generation process of the triggered emissions in "Electrons dynamics with the triggering wave and the triggered emission" section and the duration time of the triggering wave for formation of the triggered emissions in "Interaction time for the generation of triggered emissions" section. Finally, we summarize and discuss our simulation results in "Summary and discussion" section.

Simulation model

A one-dimensional particle-in-cell simulation in a uniform magnetic field is performed to reproduce whistler-mode triggered emissions. We use the 1-D version of Kyoto university ElectroMagnetic Particle cOde (KEMPO) developed by Omura and Matsumoto (1993), Omura (2007), and Nogi et al. (2020). In the code, Maxwell's equations, including both electromagnetic and electrostatic components, and relativistic equations of motion are solved self-consistently. Figure 1 shows a schematic illustration of the simulation model and the coordinates axes in the simulation system. We set a uniform background magnetic field along the x-direction, and a triggering wave is excited from the center of the simulation system. The amplitude of the triggering wave is set as $B_{wi} = 5.0 \times 10^{-3}\, B_0$, where B_0 is the background magnetic field, and the frequency of the triggering wave is $\omega = 0.3\ \Omega_e$, where Ω_e is the electron cyclotron frequency.

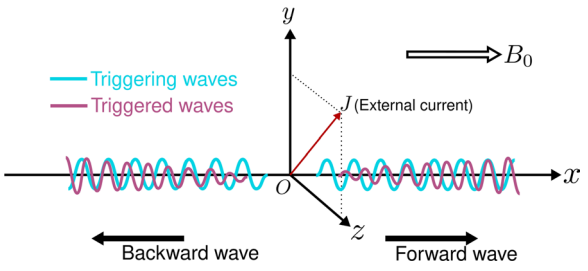

Fig. 1 Schematic illustration of the simulation model and the coordinates of the simulation system

For a plasma environment, we assume two species of particles, cold electrons and energetic electrons. As the initial condition, cold electrons have a bi-Maxwellian distribution and energetic electrons have a subtracted-Maxwellian distribution in the momentum space $(u_\parallel, u_\perp)$ which is defined as $u_\parallel = \gamma v_\parallel$ and $u_\perp = \gamma v_\perp$, where $\gamma = [1 - (v_\parallel^2 + v_\perp^2)/c^2]^{-1/2}$. The subtracted-Maxwellian distribution in the simulation is given by the following equation:

$$F(u_\parallel, u_\perp) = C_N \exp\left(-\frac{u_\parallel^2}{2U_{t\parallel}^2}\right)\frac{1}{1-\beta} \left\{\exp\left(-\frac{u_\perp^2}{2U_{t\perp}^2}\right) - \exp\left(-\frac{u_\perp^2}{2\beta U_{t\perp}^2}\right)\right\}, \tag{1}$$

where C_N is a normalization coefficient, and β is a subtraction ratio. All particles are randomly distributed in position as an initial state. The plasma frequency of cold electrons ω_{pe} is set as $2.0\ \Omega_e$ which is the typical value outside the plasmapause, and the density ratio N_h/N_c of energetic electrons to cold electrons is 0.01. The parallel and perpendicular thermal momenta of energetic electrons are $U_{t\parallel} = 0.30\, c$ and $U_{t\perp} = 0.35\, c$, where c is the speed of light, and the energy range of the energetic electrons is 1–200 keV. The resonance energy estimated from the average perpendicular momentum for the subtracted-Maxwellian distribution is 114 keV. The linear growth rate is maximized at $\omega = 0.292\ \Omega_e$, and the value is 7.45×10^{-4} calculated by the plasma linear dispersion solver KUPDAP (Sugiyama et al. 2015).

To inject whistler-mode waves into the simulation system, we use right-handed polarized external currents. Yagitani et al. (1992) have derived the relation between the external current and the magnitude of the radiated electromagnetic field. Assuming right-handed polarized external currents, we obtain the amplitude of the magnetic field B_{wi} for the triggering wave as:

$$B_{wi} = \frac{\mu_0 J_0}{2}, \tag{2}$$

where μ_0 is the vacuum permeability, and the J_0 is the amplitude of the external current. To avoid excitation of unintended wave modes, the amplitude of the external current varied smoothly at the beginning and end of the

injection time by using the sigmoid function. The amplitude of the external currents is written as:

$$J(t) = \frac{J_0}{2}\left\{\tanh\left(\frac{t-t_b}{T_b}\right) - \tanh\left(\frac{t-t_e}{T_e}\right)\right\}, \quad (3)$$

where t_b is the beginning time of oscillation, t_e is the ending time of oscillation, T_b and T_e are time scales of the amplitude variation. In this paper, we set $T_b = 4\ \Omega_e^{-1}$ and $T_e = 8\ \Omega_e^{-1}$. The duration time of the triggering wave in the simulation is defined as $\Delta t = t_e - t_b$, and we set $t_b = 20\ \Omega_e^{-1}$ as a constant value.

The periodic boundary conditions for the field and particles are applied in the simulation. We ensure that our simulations terminate before the triggering wave reaches the boundary. When an electron passes through the boundary, its gyro-phase is randomized so that generation of new emissions from the phase-organized electrons is prevented beyond the boundary.

Detailed parameter settings are shown in Table 1. We conduct four cases of simulations with different duration times of the triggering wave injection. The duration times $\Delta t = 980, 230, 105, 40\ \Omega_e^{-1}$ correspond to Cases 1, 2, 3, and 4, respectively. Comparing these cases, we discuss the characteristics of triggered emissions and the duration time necessary for the generation of triggered emissions. Using Cases 1 and 2, we describe the generation mechanism of the triggered emission in the homogeneous magnetic field by analyzing resonant currents and electron dynamics.

Triggered emissions in a uniform magnetic field

Figure 2a–d shows the temporal and spatial evolution of magnetic field amplitude B_w of forward waves with different duration times of triggering waves $\Delta t = 980, 230, 105, 40\ \Omega_e^{-1}$. The wave magnetic field amplitude is defined as $B_w = \sqrt{B_y^2 + B_z^2}$ which is the perpendicular component in the simulation system. We use the spatial helicities of the circularly polarized waves, which are decomposed in wavenumbers by the discrete Fourier transform, to separate the forward and backward waves. In all the following analyses, we only use the forward wave information because of the spatial symmetry of the simulation settings. In Fig. 2a–c, we find that clear packets of triggered emissions are generated after the termination of the triggering wave, and the triggered emission is not generated in Fig. 2d. For the wave packet sp1 in Fig. 2a, the amplitude enhancement occurs in the triggering wave and it is difficult to determine if it is a triggering or triggered wave packet. It may also be difficult to identify a triggered wave packet in Fig. 2c. However, triggered wave packets become much clearer by eliminating the triggering wave by a band-pass filter based on the frequency information as shown in Fig. 2e–h. If the amplitude value is less than $10^{-3.5}$, it is masked as shown in white color in Fig. 2e–h. In Fig. 2e, we find that sp1 is the first subpacket of triggered emissions, and sp1 is generated in the triggering wave. The amplitude enhancement in Fig. 2a is caused by the superposition of the triggering wave and the newly triggered wave. By comparing the amplitude of the first subpacket, Case 2 takes the maximum amplitude increase for the triggered emissions in Fig. 2e–g.

Figure 3a–d shows the temporal and spatial evolution of instantaneous frequencies of forward waves with different duration times of triggering waves corresponding to Fig. 2a–d. For the calculation of instantaneous frequencies, we take the time derivatives of circularly polarized wave phases, which are determined by magnetic

Table 1 Simulation parameters

Parameter	Value
Grid size	$0.05\ c\Omega_e^{-1}$
Length of the simulation region	$1638.4\ c\Omega_e^{-1}$
Time step	$0.04\ \Omega_e^{-1}$
Simulation time	$2621.44\ \Omega_e^{-1}$
Electron charge-to-mass ratio $-e/m_0$	-1
Number of cold electrons	1,073,741,824
Number of energetic electrons	2,147,483,648
Density ratio of energetic electrons to cold electrons N_h/N_c	0.01
Thermal momenta of energetic electrons $U_{t\parallel}, U_{t\perp}$	$0.30c$, $0.35c$
Temperature anisotropy $A = T_\perp/T_\parallel - 1$	0.36
Amplitude of the triggering wave B_{wi}	$5.0 \times 10^{-3} B_0$
Frequency of the external current ω	$0.3\ \Omega_e$
Duration times of the triggering waves of Cases 1, 2, 3, 4 Δt	$980, 230, 105, 40\ \Omega_e^{-1}$

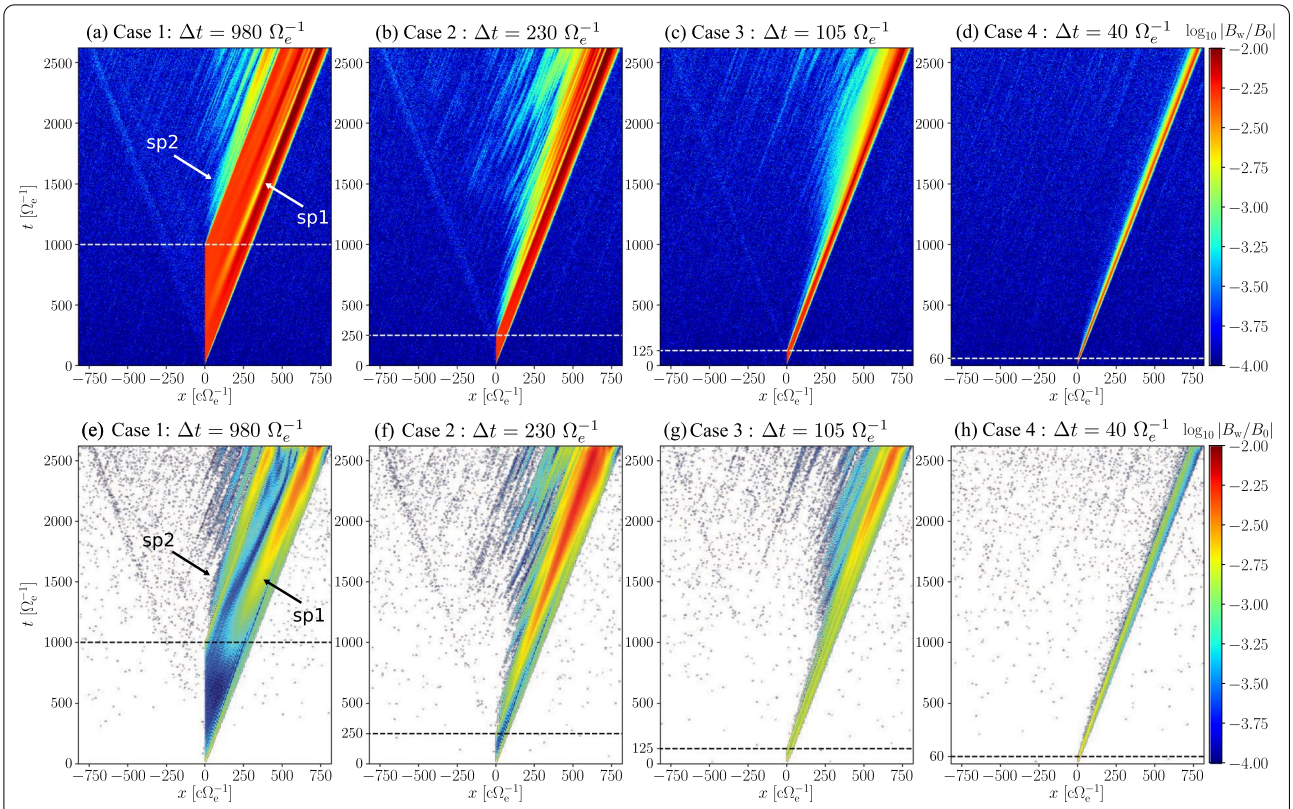

Fig. 2 Temporal and spatial evolution of magnetic field amplitudes of forward waves **a–d** with the triggering wave and **e–h** without the triggering. The duration times of the triggering wave are **a, e** 980 Ω_e^{-1}; **b, f** 230 Ω_e^{-1}; **c, g** 105 Ω_e^{-1}, and **d, h** 40 Ω_e^{-1}. White and black dashed lines indicate the termination time of the triggering wave

field components B_y and B_z of the forward waves. Since we focus on the whistler-mode triggered emissions, we apply a band-pass filter which passes the wave modes with frequencies lower than cyclotron frequency Ω_e as shown in Fig. 3a–d. In Fig. 3a–c, we find that triggered emissions are generated with frequencies higher than the triggering wave frequency $\omega = 0.3\ \Omega_e$, and Case 2 takes the maximum frequency increase.

Figure 3e–h shows the temporal and spatial evolution of instantaneous frequencies after removing triggering waves by the band-pass filter. In Fig. 3e, we find that the first subpacket sp1 has higher frequency than the triggering wave frequency. It looks like the frequency is increasing and decreasing in sp1 in Fig. 3a, however, it is caused by the superposition of two waves with different frequencies. By comparing the subpackets sp1 and sp2 in Fig. 3e, frequency increase of the subpacket sp2 is larger than that of sp1. The second subpacket sp2 is triggered by the primary triggering wave or a new triggering wave which is originated from sp1. We are unable to determine the triggering wave exactly, because the frequency of sp1 is not much different from that of the primary triggering wave.

Figure 4a shows the time evolution of magnetic field amplitudes in both Cases 1 and 2, and Fig. 4b,c shows the time evolution of spectrums with instantaneous frequencies of Cases 1 and 2, respectively. Figure 4 shows the information of wave amplitude and frequency observed at the fixed position $x = 204.8\ c\Omega_e^{-1}$. Figure 4b shows that the triggering wave have a constant frequency $\omega = 0.30\ \Omega_e$ and triggered emissions have a new frequency $\omega = 0.34\ \Omega_e$. In Fig. 4c, the spectrogram shows that the frequency gradually increases to $\omega = 0.36\ \Omega_e$ after the termination of the triggering wave.

In Case 2, the triggered emission consists of multiple small subpackets as shown in Fig. 4c, and the frequency of each subpacket is almost constant in a frame of reference moving with its group velocity as shown in Fig. 3b. We find the dispersion effect at the wavefront of the triggering wave due to the variation of the group velocities for different frequencies in Cases 1 and 2. The frequency increase is observed at the wavefront of the triggering wave in Fig. 4b , c. In Case 4, the triggering wave expands slightly in space and time because of the dispersion of the short triggering wave containing different frequencies as shown in Fig. 3d.

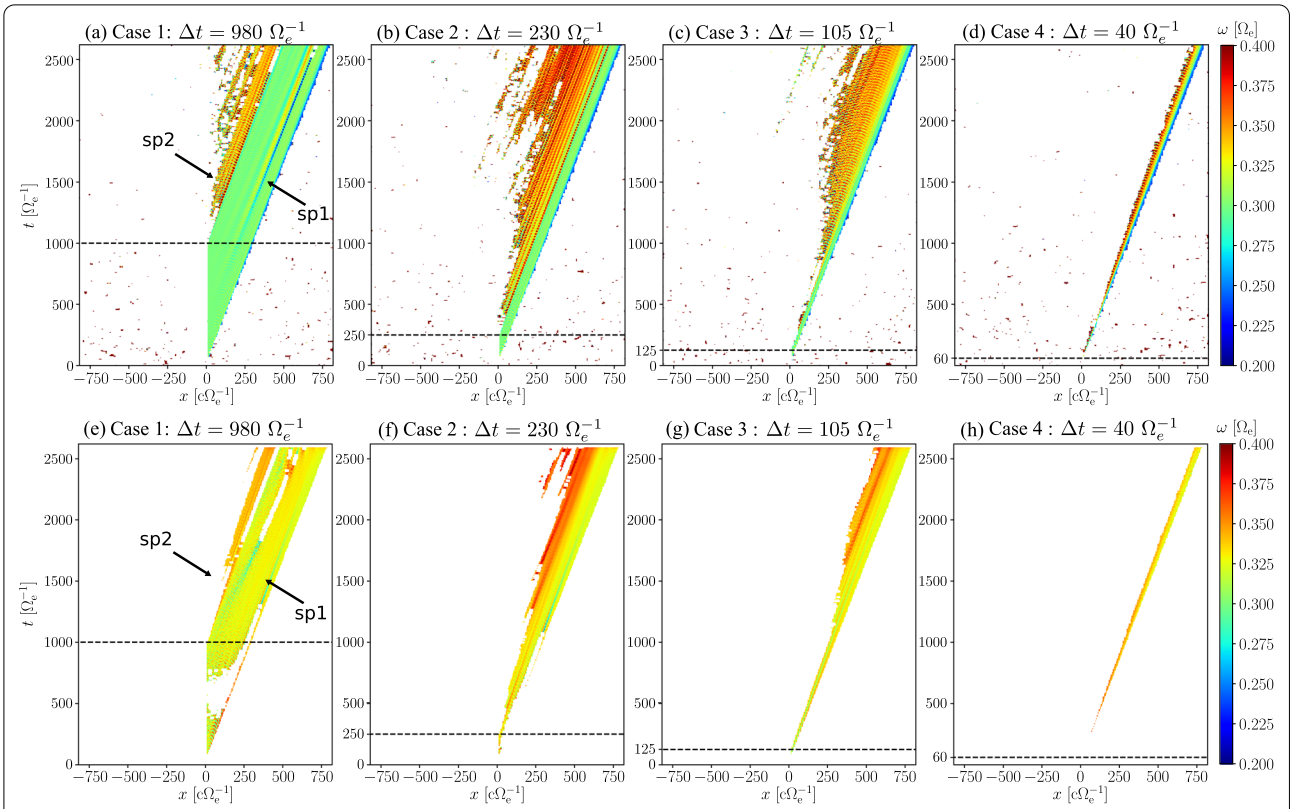

Fig. 3 Temporal and spatial evolution of instantaneous frequencies of forward waves **a–d** with the triggering wave and **e–h** without the triggering wave. The same runs are shown in Fig. 2. Black dashed lines indicate the termination time of the triggering wave

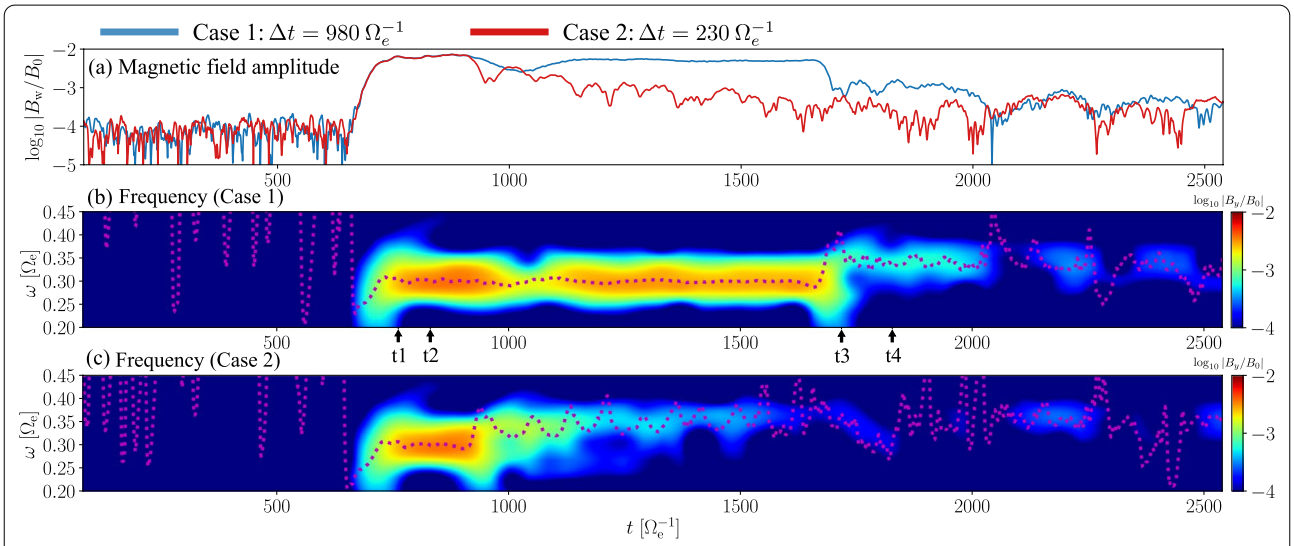

Fig. 4 Time evolution of **a** magnetic field amplitude, **b** spectrum with instantaneous frequency (Case 1) and **c** spectrum with instantaneous frequency (Case 2) observed at $x = 204.8\ c\Omega_e^{-1}$. In **b** and **c**, magenta dotted lines indicate the instantaneous frequencies. Arrows t1–t4 in **b** correspond to $t = 760,\ 829,\ 1717$, and $1826\ \Omega_e^{-1}$, respectively

Electrons dynamics with the triggering wave and the triggered emission

To understand the generation mechanism of triggered emissions in a uniform magnetic field, we analyze the dynamics of resonant electrons with the triggering wave and the triggered emission in terms of resonant currents. Resonant currents J_E and J_B are defined as currents parallel to the wave electric field and the wave magnetic field formed by resonant electrons, respectively. The wave equation and the dispersion relation with the resonant currents are written as:

$$\frac{\partial B_w}{\partial t} + V_g \frac{\partial B_w}{\partial x} = -\frac{\mu_0 V_g}{2} J_E, \tag{4}$$

$$c^2 k^2 - \omega^2 - \frac{\omega \omega_{pe}^2}{\Omega_e - \omega} = \mu_0 c^2 k \frac{J_B}{B_w}, \tag{5}$$

where V_g is the group velocity and k is the wavenumber (Omura et al. 2008). The amplitude of the wave magnetic field and the dispersion relation for the whistler-mode wave are modified by terms J_E and J_B/B_w. In Fig. 4c, the instantaneous frequency plotted by the dotted line in magenta shows the gradual increase with oscillations in the bandwidth of the wave packet. We find that the oscillation occurs in antiphase with the amplitude because of larger magnitudes of J_B/B_w in Eq. (5) with smaller B_w.

Figure 5a, b shows the temporal and spatial evolution of resonant currents $-J_E$ and J_B/B_w of the forward waves, which are calculated with reference to the total electromagnetic fields for Case 1. For the calculation of resonant currents in the simulation, we take inner products between the perpendicular velocities of electrons and the electromagnetic waves, and we integrate the inner products for the resonant electrons at different positions. In the triggering wave in Case 1, there exist the triggering wave and the triggered wave simultaneously, and we cannot properly explain the wave generation only by Fig. 5a, b, because Eqs. (4, 5) are derived under an assumption of a single wave packet. Therefore, we conducted another run with the same initial setting of Case 1 removing the wave number of the triggering wave by applying discrete Fourier transforms in space in the calculation of the resonant currents. Figure 5c, d shows the temporal and spatial evolution of resonant currents $-J_E$ and J_B/B_w of the forward waves, which are calculated with reference to the triggered waves in Case 1. From Eqs. (4, 5), we find that $-J_E > 0$ causes wave growth and $J_B/B_w < 0$ causes frequency increase. By comparing the position of sp1 and sp2 in Figs. 2e, 5c, d, we find that the triggered emissions with frequency increase are generated by the resonant currents which satisfy $-J_E > 0$ and $J_B/B_w < 0$.

We analyze the dynamics of the resonant electrons using Case 1. Figure 6a–e shows the phase space density (PSD) of the energetic electrons $g(\Delta v_\parallel, \zeta)$ observed at $x = 204.8\, c\Omega_e^{-1}$ (at the same position as shown in Fig. 4). Figure 6f–j shows the differences of the PSD of energetic electrons from the initial values of the PSD, where the differences are normalized by the initial values. The times $t = 12$, 760, 829, 1717, and 1826 Ω_e^{-1} correspond to Initial state (t0), Wavefront (t1), Triggering wave (t2), Wave end (t3), and Triggered emission (t4), respectively. Arrows on the horizontal axis in Fig. 4b indicate the times $t =$ t1–t4. The vertical axis $\Delta v_\parallel$ in Fig. 6 represents the difference between the parallel velocity of electrons $v_\parallel$ and the resonance velocity V_R calculated with the triggering wave frequency.

Figure 6a shows the initial state of the PSD. Electrons with larger negative parallel velocities have smaller PSD because electrons are initialized by Maxwellian in the parallel direction. When the wave arrives at the observation point, the PSD modulation appears in Fig. 6b. Dynamics of resonant electrons in the velocity phase space are described by the following equations:

$$\frac{d\zeta}{dt} = \theta, \tag{6}$$

$$\frac{d^2\zeta}{dt^2} = \omega_{tr}^2 (\sin\zeta + S), \tag{7}$$

where $\theta = k(v_\parallel - V_R)$, ζ is a relative phase angle between the wave magnetic field B_w and the perpendicular velocity of an electron $v_\perp$. The constant ω_{tr} is a trapping frequency which means the frequency of the oscillation of resonant electrons in the velocity phase space, and ω_{tr} is written as:

$$\omega_{tr} = \chi \left(\frac{k V_{\perp 0} e B_w}{m_0 \gamma} \right)^{\frac{1}{2}}, \tag{8}$$

where e is an elementary charge, m_0 is a mass of an electron, and $V_{\perp 0}$ is an average perpendicular velocity. χ is a dimensionless parameter given by $\chi^2 = 1/(1+\xi^2)$, where $\xi^2 = \omega(\Omega_e - \omega)/\omega_{pe}^2$, and these equations are obtained from the cold plasma dispersion relation. The parameter S is the inhomogeneity factor and determined by the frequency sweep rate $\partial\omega/\partial t$ in a uniform magnetic field. The electrons motion in the velocity phase space varies depending on whether it is inside or outside of the separatrix, which is a boundary of trapped electrons trajectories. Black dash-dotted lines in Fig. 6 indicate the separatrices calculated from simulation parameters in Table 1 and wave amplitudes and frequencies with $S = 0$

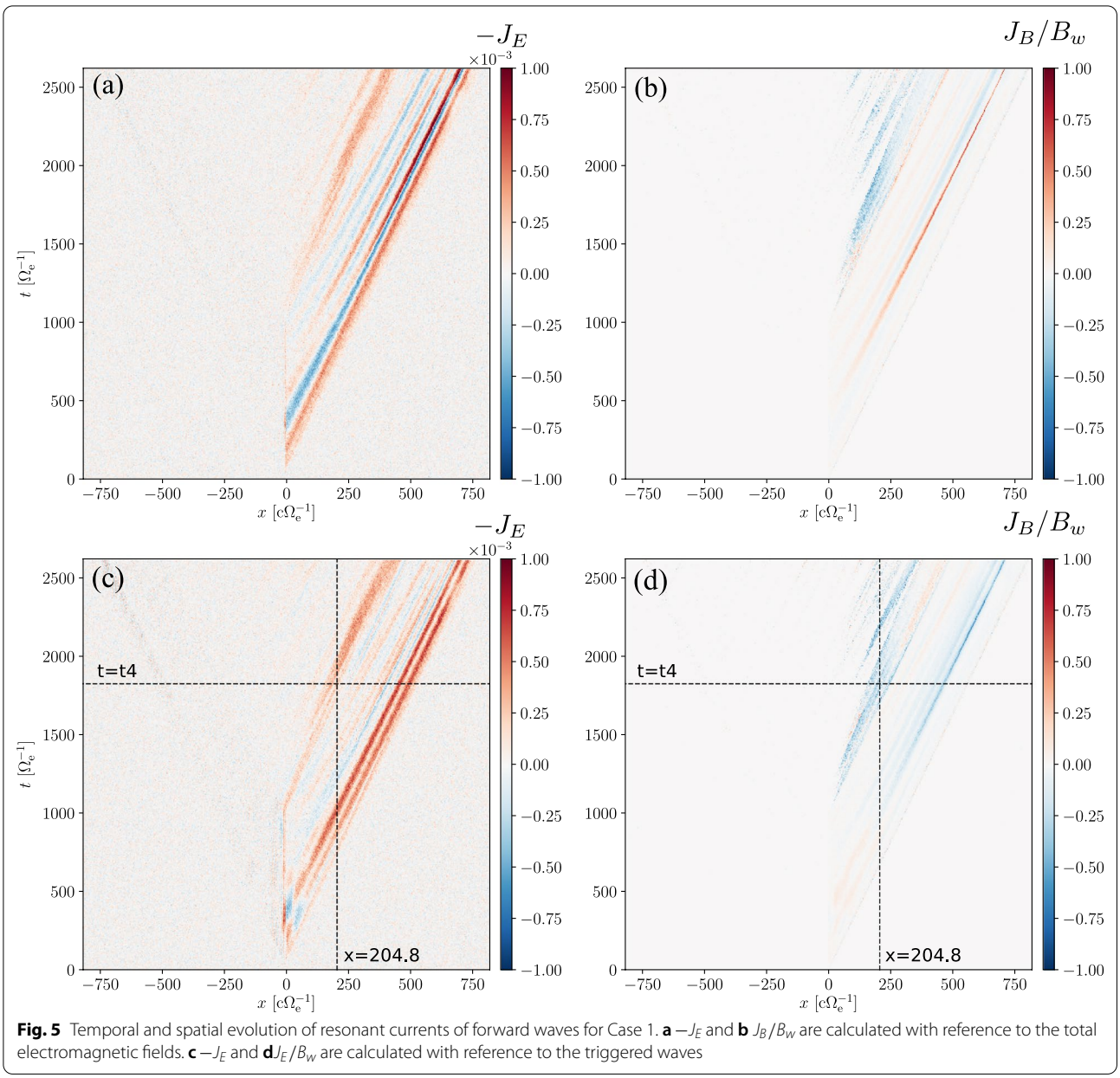

Fig. 5 Temporal and spatial evolution of resonant currents of forward waves for Case 1. **a** $-J_E$ and **b** J_B/B_w are calculated with reference to the total electromagnetic fields. **c** $-J_E$ and **d** J_E/B_w are calculated with reference to the triggered waves

and $\Delta v_\parallel = 0\,c$ for Fig. 6b, c, g, and h and $S = -0.4$ and $\Delta v_\parallel = 0.07\,c$ for Fig. 6e, j, respectively, obtained by visual inspection for reference.

By the rotation of electrons in the velocity phase space, some electrons with a large PSD around $\zeta = \pi$ move to the area close to $\zeta = 3\pi/2$, and some electrons with a low PSD around $\zeta = \pi$ move to the area close to $\zeta = \pi/2$. After this process, we find the electron depression and enhancement in Fig. 6c, h. At the triggering wave tail, we do not find the clear wave potential in Fig. 6d, i. The electron depression is uniformly distributed at $\Delta v_\parallel = 0.07\,c$. We find that the depression of resonant electrons near the dashed line moves to the upper side of the dashed line and becomes the electron hole which generate resonant currents where $-J_E$ becomes positive and J_B/B_w becomes negative in Fig. 5c, d at $t = $ t4, resulting in wave growth and frequency increase. When we find the triggered emissions, there appear trajectories of resonant electrons described by Equation (7) with $S < 0$ in Fig. 6e, j. The electron hole above the dashed line represents the generation of triggered emissions with higher frequencies than those of triggering waves.

Figure 7 shows the perpendicular velocity distribution of energetic electrons $h(v_{\perp 1}, v_{\perp 2})$ observed at

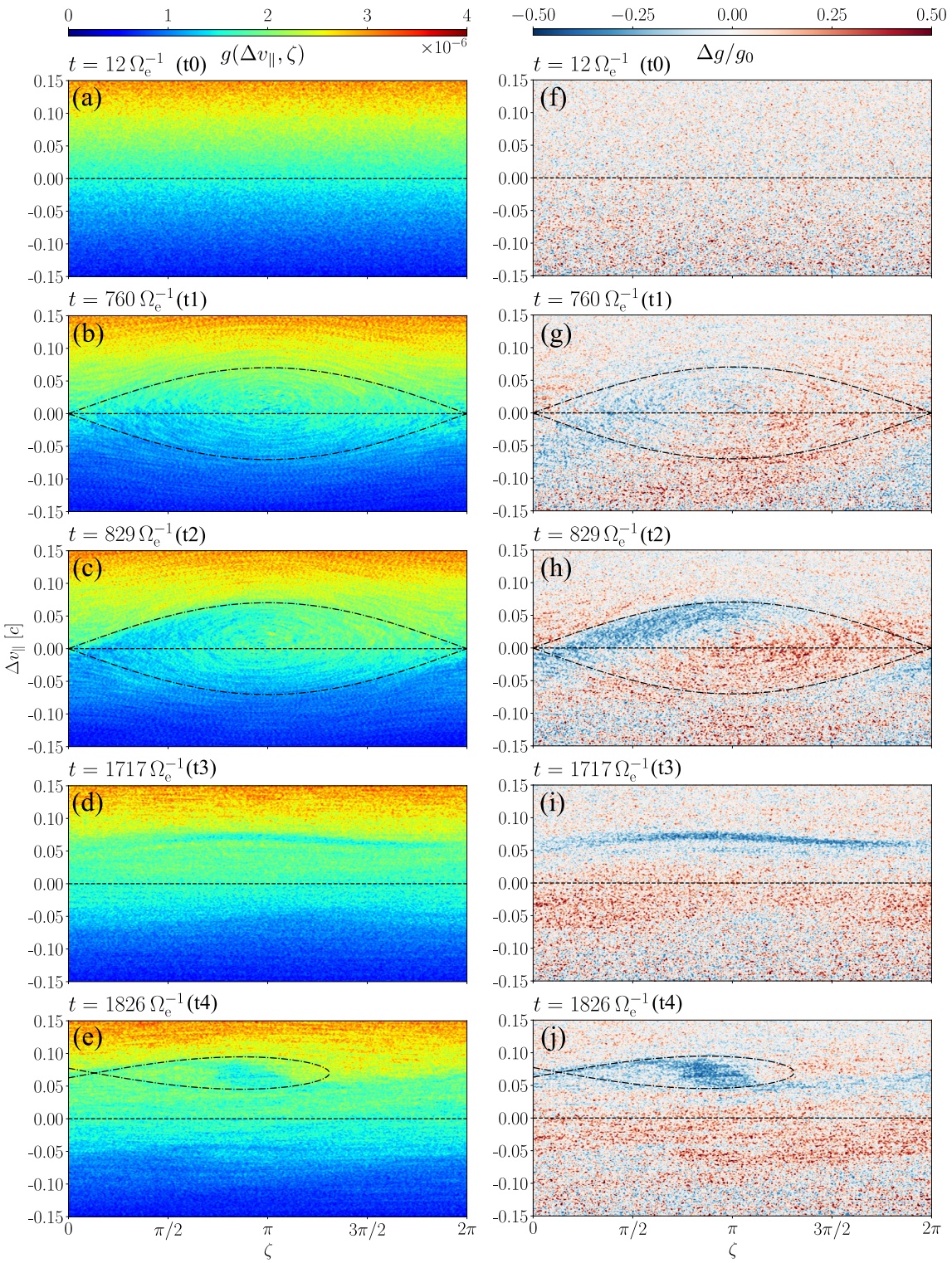

Fig. 6 PSD of the energetic electrons $g(\Delta v_\parallel, \zeta)$ observed at $x = 204.8\, c\Omega_e^{-1}$ (after integration over $x = 203.2$–$206.4\, c\Omega_e^{-1}$) and $t =$ t0–t4. **a–e** $g(\Delta v_\parallel, \zeta)$. **f–j** $\Delta g/g_0 = (g - g_0)/g_0$, where g_0 is initial values of PSD. Black dash-dotted lines indicate the separatrices of the trapped electrons and untrapped electrons with assumptions of $S = 0$ and $\Delta v_\parallel = 0\, c$ in **b**, **c**, **g**, **h**, and $S = -0.4$ and $\Delta v_\parallel = 0.07\, c$ in **e, j**

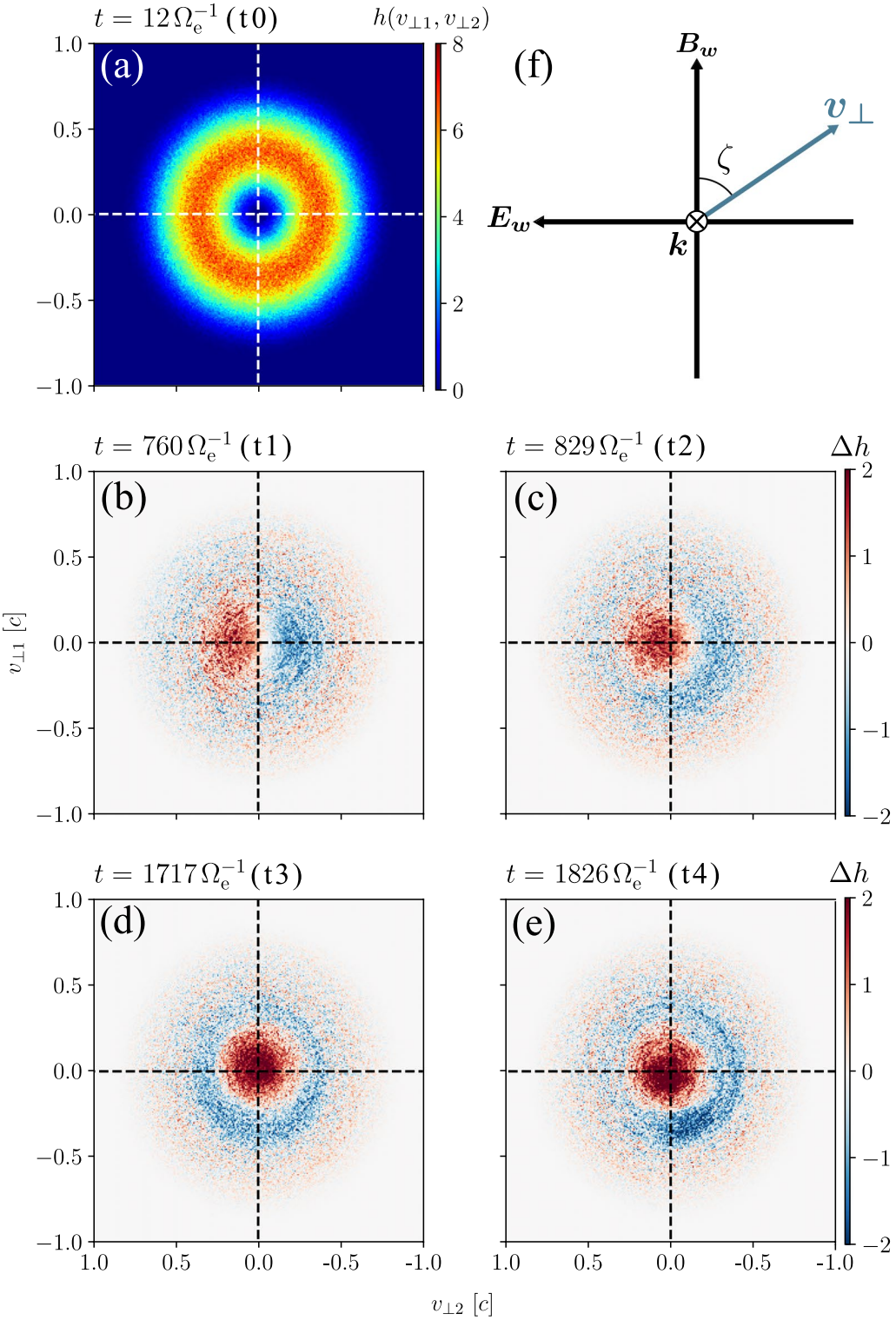

Fig. 7 Perpendicular velocity distribution of energetic electrons $h(v_{\perp 1}, v_{\perp 2})$ observed at $x = 204.8\,c\Omega_e^{-1}$ (after integration over $x = 203.2$ –206.4 $c\Omega_e^{-1}$) and $t =$ t0–t4. **a** Initial distribution h_0. **b–e** $\Delta h = h - h_0$. **f** Configuration of the wave magnetic field B_w, wave electric field E_w, wave vector k, and perpendicular velocity of an electron $v_\perp$

$x = 204.8\, c\Omega_e^{-1}$ at $t =$ t0–t4. Figure 7a shows the initial distribution, and Fig. 7b–e shows the differences of the perpendicular velocity distribution of energetic electrons from the initial distribution. We decompose the perpendicular velocity $v_\perp$ of each electron into two Cartesian components $v_{\perp 1}$ and $v_{\perp 2}$, which are the projections on the B_w and E_w directions, respectively. The schematic illustration is shown in Fig. 7f. To reduce the numerical noises, electrons with the parallel velocities, $V_R - 0.1c < v_\parallel < V_R + 0.1c$ are taken into account. This range is defined so that the trapping velocity $V_{tr} = 2\omega_{tr}/k$ is within the range.

At the wavefront (Fig. 7b), phase-bunching occurs in the direction of E_w. The rotation of resonant electrons in the velocity phase space as seen in Fig. 6b leads to the PSD decrease at $\zeta = \pi/2$ and the PSD increase at $\zeta = 3\pi/2$ from the initial state. The current is formed in the direction of E_w as $-J_E > 0$ by phase-bunched electrons, and the kinetic energy of energetic electrons is transferred to the electromagnetic waves. After the wavefront (Fig. 7c), areas of low density move to the lower right, and areas of the high density (the phase-bunched electrons) move to the center of the figure. The phase-bunched electrons and the areas of low density are related to the PSD enhancement and depression in Fig. 6h. In Fig. 7e, considering only the contribution of the electron hole, we find that the resonant currents become $-J_E > 0$ and $J_B < 0$ which are identical to the conditions for the generation of triggered emissions with frequency increase.

In the previous paragraphs, we described the electron dynamics based on the set of parameters $(v_\parallel, \zeta)$ in Fig. 6 and $(v_{\perp 1}, v_{\perp 2})$ in Fig. 7, which are two components of the three-dimensional velocity space. Figure 8 shows the velocity distribution function (VDF) of energetic electrons $f(v_\parallel, v_\perp)$ observed at $x = 204.8\, c\Omega_e^{-1}$ and $t =$ t0–t4. Figure 8a shows the initial VDF, and Fig. 8b–e shows the differences of the VDF of energetic electrons from the initial VDF. At the wavefront, while the phase-bunching occurs, the substantial variation of the VDF is not observed in Fig. 8b. After the end of the phase-bunching stage, we find that the electrons are scattered in Fig. 8c. Comparing Fig. 7c with Fig. 8c, we find that scattered electrons are originated from the phase-bunched electrons. The electron scattering is caused by the energy transfer from the electrons to the waves in the presence of $-J_E > 0$. In Fig. 8e, we find the position of depletion move to the direction in which the absolute value of $v_\parallel$ becomes smaller. This result indicates that the resonance velocity is shifted because of the frequency variation from the triggering wave ($\omega = 0.3\Omega_e$) to the triggered waves ($\omega > 0.3\Omega_e$).

Interaction time for the generation of triggered emissions

We discuss the duration time of the triggering wave required to trigger new emissions through the interaction between the triggering wave and counter-streaming electrons with resonance velocity $V_R = (\omega - \Omega_e/\gamma)/k$. The distance over which resonant electrons can interact with the triggering wave is $(V_g - V_R)T_{int}$, where T_{int} is an interaction time. A triggering wave propagating with the group velocity V_g has a maximum width of wavepacket as $V_g \Delta t$, where Δt is the duration time of the triggering wave injection. In the simulation, the frequency of the triggering wave is constant and the resonance velocity of an electron is also constant. Electrons with the resonance velocity always satisfy the resonance condition and they keep interacting in the triggering wave packet. Thus, we define the interaction time T_{int} as

$$T_{int} = \frac{V_g \Delta t}{V_g - V_R}\left(1 - \frac{V_g V_R}{c^2}\right), \tag{9}$$

equating the interaction distance and the width of the triggering wave packet, where the relativistic effect is included (Omura et al. 2019). Figure 9 shows a schematic illustration of motion of a resonant electron interacting with the triggering wave. Using a time-scale factor $\tau = T_{int}/T_{tr}$, where the nonlinear trapping period is written as $T_{tr} = 2\pi/\omega_{tr}$, we estimate the duration time of the triggering wave required to generate triggered emissions as:

$$\Delta t = \frac{V_g - V_R}{V_g}\tau T_{tr}\left(1 - \frac{V_g V_R}{c^2}\right)^{-1}. \tag{10}$$

In the simulation, we use the subtracted-Maxwellian distribution for the energetic electrons. The average perpendicular momentum for the subtracted-Maxwellian distribution $U_{\perp 0}$ is written by Omura (2021) as:

$$U_{\perp 0} = \sqrt{\frac{\pi}{2}}\left(\frac{1 - \beta^{3/2}}{1 - \beta}\right)U_{t\perp}. \tag{11}$$

Assuming that the resonant electrons have the average perpendicular velocity $V_{\perp 0} = U_{\perp 0}/\gamma$, we obtain the explicit solution of resonance velocity as:

$$\tilde{V}_R = \frac{\tilde{\omega}_u^2 - \sqrt{\tilde{\omega}_u^4 + \left(\tilde{\omega}_u^2 + \tilde{V}_p^2\right)\left(1 - \tilde{\omega}_u^2\right)}}{\tilde{\omega}_u^2 + \tilde{V}_p^2}\tilde{V}_p, \tag{12}$$

where $\tilde{V}_R = V_R/c$, $\tilde{V}_p = V_p/c = \chi\xi$, $\tilde{\omega}_u^2 = (1 + \tilde{U}_{\perp 0}^2)\tilde{\omega}^2$, $\tilde{U}_{\perp 0} = U_{\perp 0}/c$, and $\tilde{\omega} = \omega/\Omega_e$.

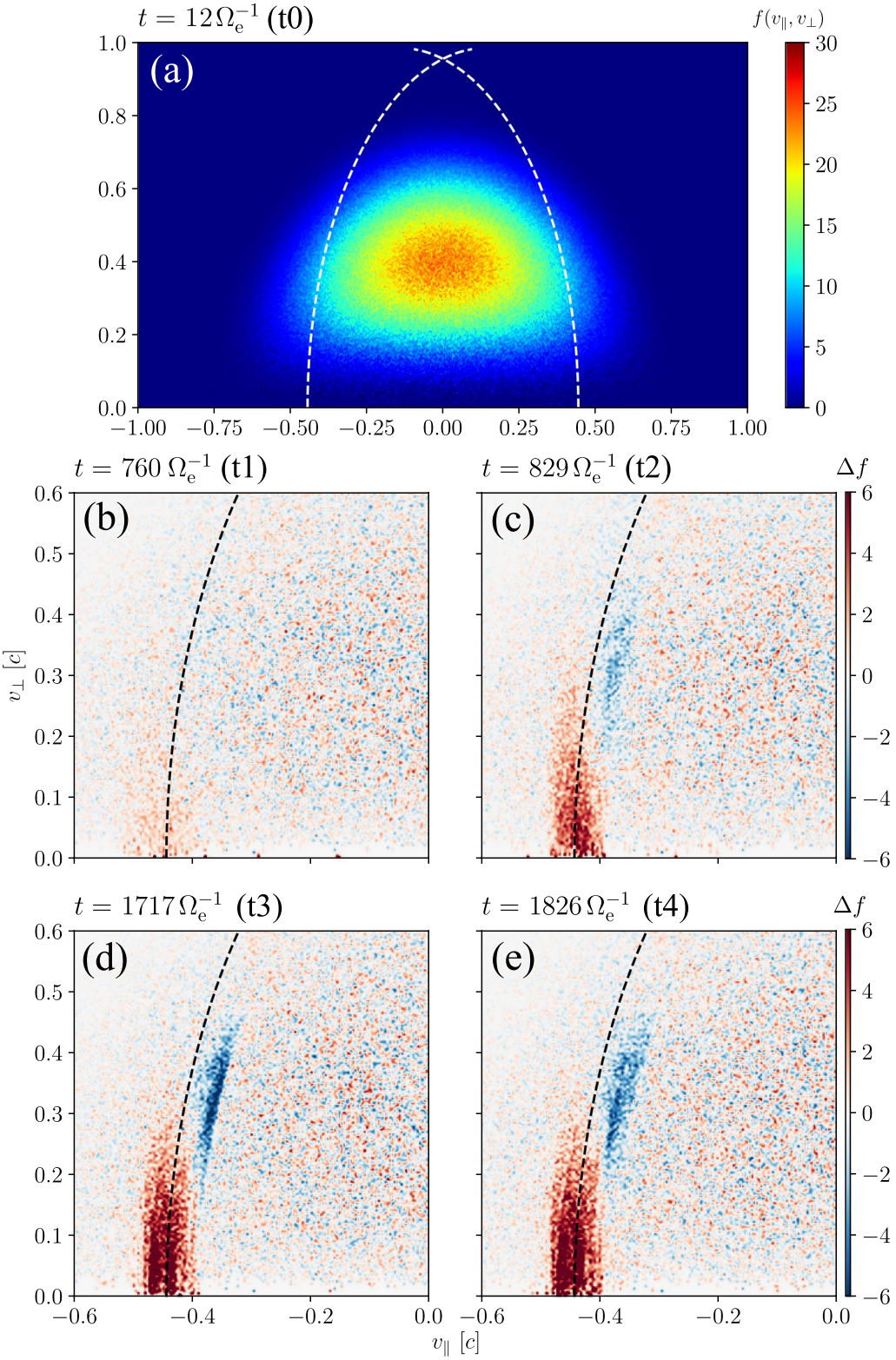

Fig. 8 VDF of energetic electrons $f(v_\parallel v_\perp)$ observed at $x = 204.8\ c\Omega_e^{-1}$ (after integration over $x = 203.2$–$206.4\ c\Omega_e^{-1}$) and $t =$ t0–t4. **a** Initial VDF f_0. **b**–**e** $\Delta f = f - f_0$. White and black dashed curves indicate the resonance velocity of the triggering wave

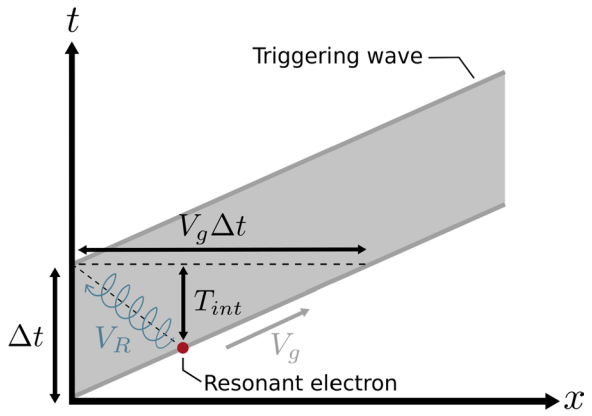

Fig. 9 Schematic illustration of motion of a resonant electron interacting with the triggering wave packet

Substituting simulation parameters of Table 1 into Eq. (12), we have resonance velocity as $V_R = -0.385\,c$ in the simulation with $V_{\perp 0} = 0.428\,c$. We also calculate the duration time of the triggering wave as $\Delta t = 268\,\Omega_e^{-1}$ from Eq. (10) with $\tau = 1$, therefore, we obtain $\tau = 3.7$ in Case 1 ($\Delta t = 980\,\Omega_e^{-1}$), $\tau = 0.86$ in Case 2 ($\Delta t = 230\,\Omega_e^{-1}$), $\tau = 0.39$ in Case 3 ($\Delta t = 105\,\Omega_e^{-1}$) and $\tau = 0.15$ in Case 4 ($\Delta t = 40\,\Omega_e^{-1}$). Omura and Nunn (2011) show that τ is in the range of 0.25–1.0. The nonlinear interaction process of forming resonant currents takes place within a single rotation of resonant electrons in the velocity phase space. We find that Case 3 has τ in the typical range and Case 4 does not have sufficient time of interaction to form resonant currents which generate triggered emissions. The electron dynamics of 1/4 rotation in the velocity phase space as in Fig. 6b causes the efficient wave–particle interaction and this supports $\tau \geq 0.25$.

Summary and discussion

We performed an electromagnetic particle simulation of triggered emissions in a uniform magnetic field with different duration times of the triggering wave. The major findings are summarized below:

- The first subpacket of triggered emissions with frequency increase is reproduced in a homogeneous magnetic field through formation of an electron hole in the velocity phase space.
- The electron hole is formed by the nonlinear trapping of resonant electrons in the packet of the triggering wave.
- We obtain the duration time of the triggering wave necessary for the formation of the electron hole.

We have evaluated the interaction time of counter-streaming resonant electrons in a triggering wave packet with a finite width. We conducted 4 runs with different duration times of the triggering pulse, 980, 230, 105, and 40 Ω_e^{-1}, which correspond to cases with interaction times, 370%, 86%, 39%, and 15% of the nonlinear trapping period, respectively. We found generation of triggered emissions in three cases of 370%, 86%, and 39%, which agrees with the conventional model that the nonlinear transition time, which is necessary for formation of resonant currents, is about a quarter of the nonlinear trapping period. The first subpacket of triggered emissions with frequency increase is generated by the resonant currents $-J_E > 0$ and $J_B/B_w < 0$ which is caused by an electron hole. The first subpacket propagates and becomes a new triggering wave with a new frequency. As a result of the interaction between the first subpacket and energetic electrons, the second subpacket is generated with a higher frequency than that of the first subpacket.

We found that the new wave generation process does not need the magnetic field gradient. The importance of the magnetic field gradient is whether the nonlinear wave growth will continue or not away from the generation region of triggered emissions. Self-sustaining nonlinear wave growth can take place through propagation away from the equator because the magnetic field gradient and growing wave amplitude can keep the S value effective for the nonlinear wave growth (Omura et al. 2009). In Fig. 2, we find that triggered waves grow convectively through propagation because of the linear growth rate, but much larger convective growth is expected if we include the magnetic field gradient in the simulation (Nogi and Omura 2022).

In the present simulation, we focused on the initial stage of the generation process of the triggered emissions with the relatively short triggering wave packets and short simulation time, and we found the generation of the first and second subpackets. This result suggests that the subpackets forms continuously with longer triggering wave packet and longer simulation time even in the homogeneous magnetic field. Possible generation of continuous subpackets with increasing frequencies is left as a future study.

Abbreviations

PSD:: Phase space density; VDF:: Velocity distribution function.

Acknowledgements

The computer simulation was performed on the KDK computer system at the Research Institute for Sustainable Humanosphere, Kyoto University. This work was supported by JSPS KAKENHI Grant JP17H06140.

Author contributions

YF conducted numerical simulations, analyzed simulation results and prepared the manuscript. TN developed the numerical simulation code. TN and

YO contributed to the discussion of the simulation results and to the revision of the manuscript. All authors read and approved the final manuscript.

Funding
This work was supported by JSPS KAKENHI Grant JP17H06140.

Availability of data and materials
The simulation data used in this paper are obtained from KEMPO1 code (http://space.rish.kyoto-u.ac.jp/software/).

Declarations

Competing interests
The authors declare that they have no competing interests.

Received: 16 July 2021 Accepted: 15 May 2022
Published online: 18 June 2022

References

Baker D, Erickson P, Fennell J, Foster J, Jaynes A, Verronen P (2018) Space weather effects in the earth's radiation belts. Space Sci Rev 214(1):1–60. https://doi.org/10.1007/s11214-017-0452-7

Demekhov A (2011) Generation of vlf emissions with the increasing and decreasing frequency in the magnetosperic cyclotron maser in the backward wave oscillator regime. Radiophys Quantum Electron 53(11):609–622. https://doi.org/10.1007/s11141-011-9256-x

Gołkowski M, Harid V, Hosseini P (2019) Review of controlled excitation of nonlinear wave-particle interactions in the magnetosphere. Front Astronomy Space Sci 6:2. https://doi.org/10.3389/fspas.2019.00002

Helliwell RA (1988) VLF wave stimulation experiments in the magnetosphere from siple station, antarctica. Reviews Geophys 26(3):551–578. https://doi.org/10.1029/RG026i003p00551

Helliwell RA (1988) VLF wave-injection experiments from siple station, antarctica. Adv Space Res 8(1):279–289. https://doi.org/10.1016/0273-1177(88)90373-0

Helliwell RA, Carpenter DL, Inan US, Katsufrakis JP (1986) Generation of band-limited VLF noise using the siple transmitter: A model for magnetospheric hiss. J Geophys Res Space Phys 91(A4):4381–4392. https://doi.org/10.1029/JA091iA04p04381

Hikishima M, Omura Y (2012) Particle simulations of whistler-mode rising-tone emissions triggered by waves with different amplitudes. J Geophys Res Space Phys. https://doi.org/10.1029/2011JA017428

Hikishima M, Omura Y, Summers D (2010) Self-consistent particle simulation of whistler mode triggered emissions. J Geophys Res Space Phys. https://doi.org/10.1029/2010JA015860

Katoh Y, Omura Y (2006) A study of generation mechanism of VLF triggered emission by self-consistent particle code. J Geophys Res Space Phys. https://doi.org/10.1029/2006JA011704

Nogi T, Omura Y (2022) Nonlinear signatures of vlf-triggered emissions: a simulation study. J Geophys Res Space Phys 127(1):e2021JA029,82629826. https://doi.org/10.1029/2021JA029826

Nogi T, Nakamura S, Omura Y (2020) Full particle simulation of whistler-mode triggered falling-tone emissions in the magnetosphere. J Geophys Res Space Phys 125(10):e2020JA027,953,753. https://doi.org/10.1029/2020JA027953

Nunn D, Omura Y (2012) A computational and theoretical analysis of falling frequency VLF emissions. J Geophys Res Space Phys. https://doi.org/10.1029/2012JA017557

Nunn D, Manninen J, Turunen T, Trakhtengerts V, Erokhin N (1999) On the nonlinear triggering of vlf emissions by power line harmonic radiation. Annales Geophysicae 17(1):79–94, https://doi.org/10.1007/s00585-999-0079-4,https://angeo.copernicus.org/articles/17/79/1999/

Omura Y (2007) One-dimensional electromagnetic particle code KEMPO1: A tutorial on microphysics in space plasmas. In *Advanced Methods for Space Simulations*, Edited by H Usui and Y Omura (Terra Sci, Tokyo, 2007) pp 1–21

Omura Y (2021) Nonlinear wave growth theory of whistler-mode chorus and hiss emissions in the magnetosphere. Earth Planets Space 73(1):1–28. https://doi.org/10.1186/s40623-021-01380-w

Omura Y, Matsumoto H (1993) KEMPO1: Technical guide to one-dimensional electromagnetic particle code. In *Computer Space Plasma Physics: Simulation Techniques and Softwares*, Edited by H Matsumoto and Y Omura, (Terra Sci, Tokyo, 1993) pp 21–65

Omura Y, Nunn D (2011) Triggering process of whistler mode chorus emissions in the magnetosphere. J Geophys Res Space Phys. https://doi.org/10.1029/2010JA016280

Omura Y, Katoh Y, Summers D (2008) Theory and simulation of the generation of whistler-mode chorus. J Geophys Res Space Phys. https://doi.org/10.1029/2007JA012622

Omura Y, Hikishima M, Katoh Y, Summers D, Yagitani S (2009) Nonlinear mechanisms of lower-band and upper-band VLF chorus emissions in the magnetosphere. J Geophys Res Space Phys. https://doi.org/10.1029/2009JA014206

Omura Y, Hsieh YK, Foster JC, Erickson PJ, Kletzing CA, Baker DN (2019) Cyclotron acceleration of relativistic electrons through landau resonance with obliquely propagating whistler-mode chorus emissions. J Geophys Res Space Phys 124(4):2795–2810. https://doi.org/10.1029/2018JA026374

Sugiyama H, Singh S, Omura Y, Shoji M, Nunn D, Summers D (2015) Electromagnetic ion cyclotron waves in the earth's magnetosphere with a kappa-maxwellian particle distribution. J Geophys Res Space Phys 120(10):8426–8439. https://doi.org/10.1002/2015JA021346

Sun J, Chen L, Wang X, Boardsen S, Lin Y, Xia Z (2020) Particle-in-cell simulation of rising-tone magnetosonic waves. Geophys Res Lett 47(18):e2020GL089,67. https://doi.org/10.1029/2020GL089671

Trakhtengerts VY, Demekhov AG, Hobara Y, Hayakawa M (2003) Phase-bunching effects in triggered vlf emissions: Antenna effect. J Geophys Res Space Phys. https://doi.org/10.1029/2002JA009415

Yagitani S, Nagano I, Omura Y, Matsumoto H (1992) Comparison between particle simulation and full-wave analysis for wave propagation in a nonuniform plasma. Radio Sci 27(4):449–462. https://doi.org/10.1029/92RS00854

Publisher's Note